Electrochimica Acta 296 (2019) 907–915

Contents lists available at ScienceDirect

Electrochimica Acta

journal homepage: www.elsevier.com/locate/electacta

Biological cell template synthesis of nitrogen-doped porous hollow carbon spheres/MnO_2 composites for high-performance asymmetric supercapacitors

Wei Du [a,*], Xiaoning Wang [a], Jie Zhan [b], Xueqin Sun [a], Litao Kang [a], Fuyi Jiang [a], Xiaoyu Zhang [a], Qian Shao [c], Mengyao Dong [d,e], Hu Liu [e], Vignesh Murugadoss [d], Zhanhu Guo [d]

[a] School of Environment and Material Engineering, Yantai University, Yantai, 264005, Shandong, China
[b] State Key Laboratory of Crystal Materials, Shandong University, Jinan, 250100, Shandong, China
[c] College of Chemical and Environmental Engineering, Shandong University of Science and Technology, Qingdao, 266590, China
[d] Integrated Composites Laboratory (ICL), Department of Chemical & Biomolecular Engineering, University of Tennessee, Knoxville, TN, 37996, USA
[e] School of Materials Science and Engineering, Key Laboratory of Materials Processing and Mold (Zhengzhou University), Ministry of Education, National Engineering Research Center for Advanced Polymer Processing Technology, Zhengzhou University, Zhengzhou, 450002, Henan, China

A R T I C L E I N F O

Article history:
Received 21 August 2018
Received in revised form
23 October 2018
Accepted 11 November 2018
Available online 19 November 2018

Keywords:
Asymmetric supercapacitor
Biological cell template
Carbon material
Manganese dioxide
Composite

A B S T R A C T

Nitrogen-doped porous hollow carbon spheres were fabricated via hydrothermal pre-carbonization and pyrolysis carbonization using yeast cell templates. After that, the MnO_2 nanowires were deposited by the *in-situ* hydrothermal reaction. By controlling the reaction concentration, various MnO_2 nanostructures with different morphologies and electrochemical properties were obtained. The as-prepared sample exhibited an ultrahigh specific capacitance of 255 F g^{-1} at a current density 1 A g^{-1} in 1 M Na_2SO_4 electrolyte. The MnO_2/HCS-30 material was used as the positive electrode, and the HCS was used as the negative electrode to assemble the asymmetric supercapacitor. The maximum energy density operating at the 2.0 V voltage window is 41.4 Wh kg^{-1} at a power density of 500 W kg^{-1} and still maintains 23.0 Wh kg^{-1} at a power density of 7901 W kg^{-1}. Moreover, it displayed excellent cycle stability, retained approximately 93.9% of the capacitance after 5000 cycles. This work innovatively combines biomass and energy, provides an environmentally benign strategy and new insights for the preparation of electrode materials.

1. Introduction

Nowadays, the exploration and utilization of renewable and sustainable energy sources such as hydropower, wind energy, tidal energy, electrochemical energy, and solar energy are greatly relieving the heavy burdens on current energy and environmental issues [1–16]. However, since the aforementioned readily available and sufficient energy sources are intermittent in nature, it is extremely urgent to develop stable electrochemical energy storage (EES) systems (such as fuel cells, supercapacitors, and rechargeable batteries) to promote the effective use of these renewable power sources [17,18]. Among these EES systems, supercapacitors have become more appealing due to their exclusive characteristics such as high power density (>10 kW kg^{-1}), long-term cycling stability (>100 000 cycles), and low maintenance cost [19–21]. Asymmetric supercapacitor (ASC) has a higher energy density because the complementary potential range extends the operating voltage window to give more and more applications [22].

For ASC devices, selecting/designing material systems combining all the advantages of each material component are considered as an ingenious approach [23]. MnO_2 is a typical transition-metal oxide which has been widely used as a positive electrode material due to its abundant reserves, low toxicity and high theoretical specific capacitance (1370 F g^{-1}) [24]. The mechanism of MnO_2 pseudocapacitive behavior can be attributed to the single-electron transfer of Mn^{4+}/Mn^{3+} redox system [25]. The development of MnO_2-based electrodes is still hindered by some inherent drawbacks, including low ionic diffusion constant (10^{-13}

* Corresponding author.
E-mail address: duwei@ytu.edu.cn (W. Du).

https://doi.org/10.1016/j.electacta.2018.11.074

$cm^2\ V^{-1}\ s^{-1}$), poor conductivity (10^{-5} to 10^{-6} S cm^{-1}) and large volume variations which make it difficult to achieve satisfying energy storage performance [26]. Therefore, integrating MnO_2 with high conductive substrate has been devoted to improve the energy storage performance [27]. For example, many research groups combined MnO_2 with carbon-based materials (such as active carbon, carbon fibers, graphene, nanotubes and carbon spheres) and other metal oxide materials (such as NiO, Co_3O_4, NiO/Ni$(OH)_2$ and TiO_2) [28–30]. Among these carbon-based materials, hollow carbon spheres have received special attention due to their unique spatial morphology, high chemical and thermal stability, large voids and high specific surface area [28]. In addition, it is worth mentioning that heteroatom-doped (N, O, B and P) carbon spheres can induce the surface faradaic reactions by increasing the charge mobility of negative charges on the surface of carbon material, meanwhile, high performance and long cycle life are maintained [31]. Combining the advantages of nitrogen doping and hollow carbon spheres, we have been inspired to use yeast cells as biological templates to prepare electrode materials with unique structures and environmental friendliness for superior energy storage.

Yeast cells are common unicellular microorganisms with a spherical shape, and are widely used in wine, food, medicine, feed, cosmetics and other fields [32]. In recent years, the annual production of yeast has exceeded 3 million tons with the increase in the connection between the yeast industry and human life [33–35]. It is worth noting that the yeast-rich eutrophic wastewater is becoming an inevitable problem affecting the development of the fermentation industry [36]. With the exploration of organic wastewater separation technology (such as membrane separation, chemical precipitation, concentration and centrifugation, etc.), the ingenious combination of yeast wastewater and new energy is a sensible way to solve environmental pollution while developing new types of energy storage materials [37]. The treated yeast formed a carbon sphere material having an amorphous structure, a hollow porous morphology and self-doping of heteroatoms [38–42]. However, its application for superapacitor electrode has not been studied and their practical applications as a two-electrode electrode has not been reported yet.

In this work, yeast cells were selected as biological templates to synthesize nitrogen-doped porous hollow carbon spheres. Yeast templates are known to be inexpensive and easy to produce, and the numerous functional groups on the cell membrane make them possible to be used as templates [43]. Based on these, the MnO_2/nitrogen-doped porous hollow carbon sphere composites were synthesized by in-situ hydrothermal deposition. The specific capacitance reached 255 F g^{-1} at the current density of 1 A g^{-1} in a three-electrode system. For ASC, the maximum energy density operating at the 2.0 V voltage window is 41.4 Wh kg^{-1} at a power density of 500 W kg^{-1} and still maintains 23.0 Wh kg^{-1} at a power density of 7901 W kg^{-1}. In addition, it is worth mentioning that the prepared electrode material is prepared from a renewable biological template under an environment-friendly atmosphere, which represents a simple, low-cost and green storage device production route.

2. Experimental section

2.1. Materials

The yeast powder was purchased from Angel Yeast Co., Ltd., China. All chemical reagents, including glucose, potassium permanganate ($KMnO_4$), glutaraldehyde (50%) and ethanol are analytical grade.

2.2. Synthesis of nitrogen-doped porous hollow carbon spheres

Nitrogen doped porous hollow carbon spheres were synthesized by a modified method according to the literature [40]. Briefly, the yeast powder (1 g) was firstly incubated in 0.2 M glucose aqueous solution at a constant temperature of 38 °C for 30 min in order to activate and disperse yeast. Then the activated yeast was washed with deionized (DI) water and ethanol. Subsequently, the washed yeast cells were dispersed in 60 mL 5% glutaraldehyde aqueous solution by sonication. In the hydrothermal pre-carbonization process, the above solution was transferred to a 100 mL Teflon-lined stainless-steel autoclave and heated at 180 °C for 5 h. The resulting product was vacuum filtered, washed three times with DI water and ethanol, and thoroughly dried at 60 °C to obtain a brown powder. Finally, the dried brown powder was carbonized at 850 °C for 2 h under nitrogen flow (200 mL min^{-1}) with a heating rate of 5 °C min^{-1} to synthesize hollow carbon spheres. The resultant sample was named as HCS.

2.3. Synthesis of MnO_2/N-porous hollow carbon spheres

A simple one-step hydrothermal method was used to prepare the MnO_2/carbon sphere hollow structure. Firstly, 60 mg as-prepared HCS was ultrasonically dispersed in 40 mL of 20 mM $KMnO_4$ aqueous solution. Then, this aqueous solution was transferred to a Teflon-lined stainless-steel autoclave and heated at 160 °C for 3 h. The reaction in the hydrothermal process is as follows [25]:

$$4KMnO_4 + 3C + H_2O \leftrightarrow 4MnO_2 + K_2CO_3 + 2KHCO_3 \quad (1)$$

After the reaction, the Teflon autoclave was cooled down to room temperature. The product was vacuum filtered, washed three times with DI water and ethanol, and thoroughly dried in an oven at 60 °C. The product was labeled as MnO_2/HCS-20. In the subsequent experiments, the products obtained with different reaction concentrations of $KMnO_4$ were labeled as MnO_2/HCS-30, MnO_2/HCS-40, respectively. The flow chart of the sample synthesis process was illustrated in Fig. 1.

2.4. Materials characterizations

Scanning electron microscopy (SEM, Hitachi S-4800, Japan) and transmission electron microscopy (HRTEM, JEM-2100, Japan) were used to characterize the structures and morphologies. X-ray diffraction (XRD) measurement was carried out by an X-ray diffractometer (Shimadzu-7000X, Japan) with Cu Kα radiation operated at 40 kV and 30 mA. Raman spectra were collected on Raman spectrometer (Thermo Nicolet NEXUS 670, USA) using 532 nm laser excitation. Fourier transformation infrared (FT-IR) spectra of the samples were measured from KBr sample pellets on a

Fig. 1. Schematic illustration of the overall synthesis process for MnO_2/HCS-30.

Shimadzu IR Prestige-21 (Japan). The thermogravimetric analyses (TGA) were performed on a thermogravimetric analyzer (Netzsch STA449 F3, Germany) at a heating rate of 10 °C min^{-1} under air atmosphere (air flow rate: 200 mL min^{-1}, sample mass: 10 mg). Nitrogen adsorption-desorption and pore size distributions were conducted by physisorption analyzer (Micromeritics ASAP 2020, USA) at 77 K. The surface elemental spectra were acquired by X-ray photoelectron spectroscopy (XPS, Thermo Fisher Scientific ESCALAB 250Xi, USA) with Al Kα radiation used as the excitation source.

2.5. Electrochemical measurements

The electrochemical properties of the prepared electrodes were tested in 1 M Na_2SO_4 electrolyte using a three-electrode system. The nickel foam (1 × 2 cm^2) containing active material, acetylene black and polyvinylidene fluoride (PVDF) (8:1:1 wt.%) was used as the working electrode. The active material coating on nickel foamed is approximately 3 mg. The platinum plate and saturated calomel (SCE) were used as the counter electrode and reference electrode, respectively. Cyclic voltammetry (CV), galvanostatic charge/discharge (GCD) and electrochemical impedance spectroscopy (EIS) were measured by a CHI 660E (Shanghai) electrochemical workstation. EIS measurements were performed with a frequency range from 100 kHz to 0.01 Hz at an open circuit voltage.

2.6. Assembly of ASC device and electrochemical measurements

The ASC device was assembled by using MnO_2/HCS-30 as the positive electrode, HCS as the negative electrode and Na_2SO_4 as the electrolyte. The positive and negative electrodes were prepared as described in Section 2.5. The mass loading rate of the positive and negative electrodes was determined according to the Eq. (2) [23]:

$$\frac{m_+}{m_-} = \frac{C_{s-} \times \Delta E_-}{C_{s+} \times \Delta E_+} \tag{2}$$

where C_s represents the specific capacitance, ΔE represents the potential range of each electrode and m represents the mass loading of the active material in the electrode. The subscripts + and - represent the positive and negative electrodes, respectively.

The specific capacitances were calculated based on GCD curves according to Eq. (3) [28]:

$$C_s = \frac{I \times \Delta t}{m \times \Delta V} \tag{3}$$

where I (A) is the discharge current, Δt (s) is the discharge time, ΔV (V) is the discharge voltage range. In three-electrode system, m (g) is the mass loading of active material in a single electrode. In two-electrode system, m (g) is the total mass loading of active materials based on two electrodes.

The energy density (E, Wh kg^{-1}) and power density (P, W kg^{-1}) were calculated according to Eq. (4) and Eq. (5) respectively [28]:

$$E = \frac{1}{2} C_s \Delta V^2 \frac{1}{3.6} \tag{4}$$

$$P = \frac{E}{\Delta t} \times 3600 \tag{5}$$

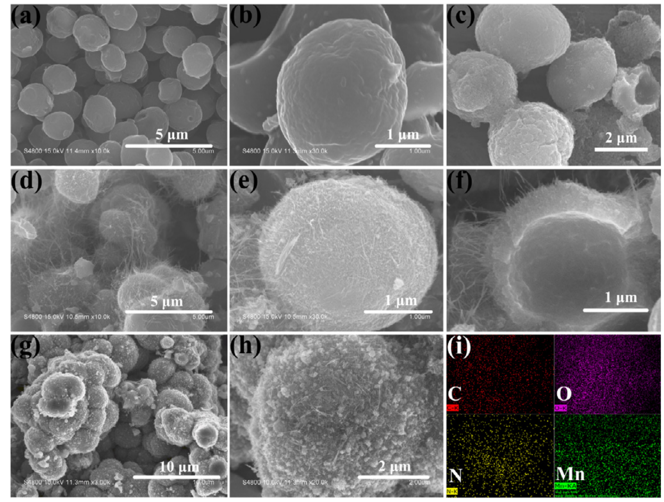

Fig. 2. SEM images of (a, b) HCS, (c) MnO_2/HCS-20, (d, e and f) MnO_2/HCS-30, (g, h) MnO_2/HCS-40, (i) EDS mapping images of C, N, O and Mn of Fig. 2e.

3. Results and discussion

3.1. Characterization of materials

SEM images of HCS and composites are shown in Fig. 2. It is noted in Fig. 2a that most of the original carbonized yeast cells exhibit a regular elliptical sphere shape. This result can be attributed to the effect of hydrothermal pre-carbonization, which coordinates the hydrolysis and carbonization speed of the cell membrane and avoids cell rupture due to direct carbonization. In addition, glutaraldehyde can be used as a protective agent in the hydrothermal pre-carbonization process to form a covalent bond between the amino group and the hydrolysis product of the polysaccharide in the cell wall, to prevent the collapse of the hollow structure and to control the integrity of the elliptical morphology [40]. The SEM image of HCS (Fig. 2b) presents an ellipsoid with a width of 2 μm and a length of 2.5 μm. As shown in SEM image of MnO_2/HCS-20 (Fig. 2c), after the hydrothermal reaction, HCS is covered by sparse MnO_2. There are still some HCS in the original state because of the lower concentration of MnO_4^-. The MnO_2/HCS-30 is covered with uniform MnO_2 nanowires as shown in Fig. 2d&e. From the SEM image of the broken yeast composites in Fig. 2f, it can be clearly seen that the composite has a shell hollow structure with a thickness of 100–200 nm. As shown in Fig. 2g&h, the surface of MnO_2/HCS-40 is covered by uniform MnO_2 particles. However, excessive deposition of MnO_2 may have an adverse effect on the electrical conductivity. Fig. 2i is an elemental distribution image of Fig. 2e, which demonstrates the presence and distribution of C, N, O and Mn and the results are consistent with the XPS analysis.

Fig. 3 presents the TEM and HRTEM images of HCS and MnO_2/HCS-30. HCS (Fig. 3a) exhibits uniform ellipsoidal morphology, which is consistent with the SEM images. The HRTEM images of the HCS (Fig. 3b&c) present a hollow internal structure and a porous shell structure. The porous structure is caused by the decomposition of some amorphous components into monosaccharides during the carbonization and hydrolysis of polysaccharides in the cell wall [40]. As can be seen from the Fig. 3d, the surface of the HCS is uniformly covered by MnO_2 nanowires. The HRTEM image (Fig. 3f) of a nanowire shows a fringe spacing of 0.24 nm, which can be ascribed to the (006) diffraction plane in birnessite-type MnO_2 and is consistent with XRD analysis.

Fig. 4a shows the XRD patterns of different samples. For HCS,

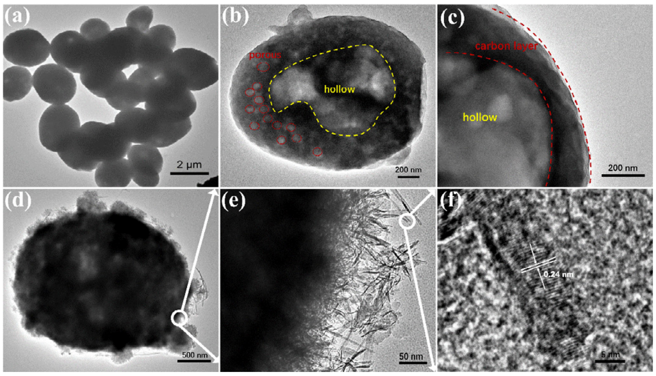

Fig. 3. TEM and HRTEM images of (a, b, c) HCS and (d, e, f) MnO_2/HCS-30.

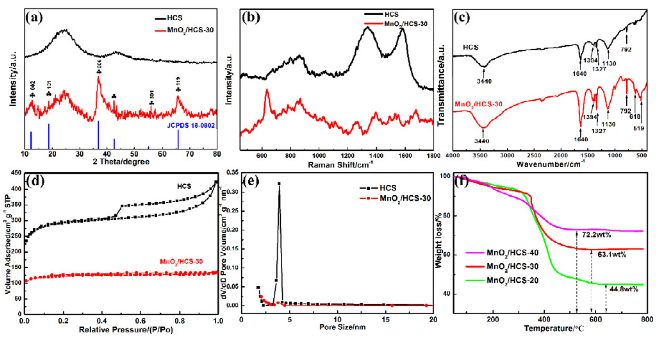

Fig. 4. (a) XRD patterns, (b) Raman spectra, (c) FT-IR spectra, (d) N_2 adsorption-desorption isotherms and (e) Pore size distributions of HCS and MnO_2/HCS-30. (f) TGA curves of MnO_2/HCS-20, 30 and 40.

two broad diffraction peaks at 25° and 43° can be attributed to the (002) and (100) reflections of the disordered carbon layer, indicating its amorphous state [44,45]. The five diffraction peaks at $2\theta = 12.5°, 18.6°, 36.9°, 55.9°$ and 65.5° in the pattern of MnO_2/HCS-30 can be indexed to (002), (101), (006), (301) and (119) crystal planes of birnessite-type MnO_2 crystalline phase (JCPDS No. 18-0802) [46].

The Raman spectra of the HCS and MnO_2/HCS-30 nanocomposites are shown in Fig. 4b. The Raman spectrum of the HCS shows two characteristic peaks located at 1340 (D band) and 1580 (G band) cm^{-1}, which can be ascribed as distinctive carbon peaks. The intensity ratio of D-to-G bands (I_D/I_G) is 1.0, revealing the partially graphitized structure of the HCS. In addition, the peaks of the two spectra at 860 cm^{-1} can be assigned to C—C stretching and CCH bending in the amorphous carbon [47]. For the spectrum of MnO_2/HCS-30, two peaks at 634 and 492 cm^{-1} are attributed to the stretching vibrations of the MnO_6 octahedra in the birnessite-type MnO_2 phase [48]. Compared to HCS, the D and G bands of MnO_2/HCS-30 are significantly reduced due to the shielding effect of MnO_2 on the surface of HCS. Fig. 4c is the FT-IR spectra of HCS and MnO_2/HCS-30 composite. The absorption peaks of HCS and MnO_2/HCS-30 at 3440 cm^{-1} and 1394 cm^{-1} correspond to the bending vibration band and stretching vibration band of —OH, respectively. Furthermore, the absorption peaks at 1640, 1327, 1130 and 792 cm^{-1} in both samples are ascribed to the stretching vibration of C═O, the stretching vibration of C═N, aromatic C—H in plane bending and C—H out of plane bending vibrations, respectively [49]. The presence of C═N groups indicates the doping of the N element. Compared with HCS, the observed two characteristic absorption peaks at 618 and 519 cm^{-1} in the MnO_2/HCS-30 are attributed to the Mn—O—Mn and Mn—O—H vibrations in MnO_2 [50]. This indicates that oxygen acts as a special node for covalent bonding of Mn atoms. The FT-IR results were verified in subsequent XPS tests.

The specific surface area and porosity were characterized by the N_2 adsorption/desorption with the Brunauer-Emmett-Teller (BET) and Barrett-Joyner-Halenda (BJH) analysis. In Fig. 4d, HCS presents type IV isotherm with a H4-type hysteresis loop, indicating a mesoporous structure. MnO_2/HCS-30 shows type I isotherm, indicating a microporous structure [27]. With the sacrifice of part of the HCS and the formation of the MnO_2 shell, the porous structure of the HCS is uniformly anchored with MnO_2, resulting in a lower specific surface area. As shown in Fig. 4e, the pore size of both samples is centered at 3.9 nm. Table 1 lists the physicochemical properties of HCS and MnO_2/HCS-30.

The composition of different composites was further investigated by TGA (Fig. 4f). It can be seen that all the TGA curves can be divided into four parts. The mass loss of the first part can be attributed to the removal of physically adsorbed water below 200 °C. The weight losses of MnO_2/HCS-20, 30 and 40 were found to be 4.1%, 5.2% and 5.9%, respectively. The second mass loss between 200 and 300 °C can be ascribed to the crystalline water in the composites, which are 2.6%, 2.3% and 5.2%, respectively. The third mass loss between 300 and 450 °C can be ascribed to the combustion of HCS and the transformation of layered structure of MnO_2 into a thermodynamically stable tunnel structure. In this process, MnO_2 decomposes to Mn_3O_4 with the release of oxygen in MnO_2. The weight losses of MnO_2/HCS-20, 30 and 40 can be calculated to be 42.7%, 26.4% and 14.6%, respectively. The final mass loss above 500 °C can be attributed to the combustion of the residual HCS and the transformation of Mn_3O_4 to Mn_2O_3, which are 5.8%, 3.0% and 2.1%, respectively. Therefore, the weight percentages of MnO_x in MnO_2/HCS-20, 30 and 40 composites were 44.8%, 63.1% and 72.2%. In other words, the content of MnO_x increases with the increase in the concentration of MnO_4^- [25].

To obtain more abundant information of surface functional groups, XPS measurements were performed on the HCS and MnO_2/HCS-30. The survey XPS spectra of HCS and MnO_2/HCS-30 (Fig. 5a) reveal the presence of C, N, O and C, N, O, Mn elements, respectively. The percentages of different elements in HCS and MnO_2/HCS-30 are shown in Table 1. The high-resolution C 1s spectrum (Fig. 5b) of HCS exhibits two peaks: C—C (284.6 eV) and C—N (285.7 eV) [51]. Fig. 5c shows the C1s high-resolution XPS spectrum of MnO_2/HCS-30 with the curve fitted with binding energies of C—C (284.7 eV), C—O (286.1 eV), and O═C—O (288.2 eV). The high-resolution N 1s spectrum of HCS was divided into four peaks (Fig. 5d) centered at 398.2, 399.3, 400.8, and 402.2 eV, corresponding to the pyridinic (N-6), pyrrolic or pyridonic (N-5), quaternary (N-Q), and oxidized (N-X), respectively [52]. Compared to the N 1s spectrum of HCS,

Table 1
Physicochemical properties of the HCS and MnO_2/HCS-30.

Sample	S_{BET} ($m^2\ g^{-1}$)	S_{meso} ($m^2\ g^{-1}$)	S_{mic} ($m^2\ g^{-1}$)	$V_{total\ pore}$ ($cm^3\ g^{-1}$)	Elemental Composition (XPS) [at%]			
					C	N	O	Mn
HCS	912	229	671	0.57	74.18	3.43	22.39	–
MnO_2/HCS-30	379	71	299	0.21	23.22	1.40	51.28	24.10

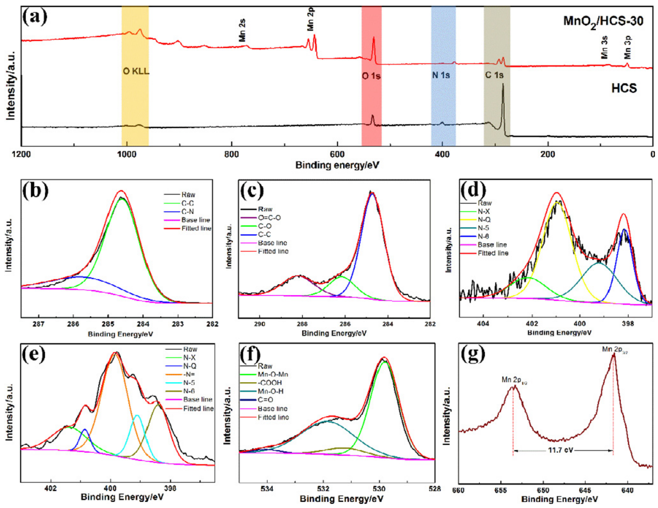

Fig. 5. (a) XPS spectra of the HCS and MnO_2/HCS-30, (b, d) High resolution C 1s, N 1s XPS spectra of HCS, (c, e, f, g) High resolution C 1s, N 1s, O 1s and Mn 2p XPS spectra of MnO_2/HCS-30.

MnO_2/HCS-30 (Fig. 5e) shows more diversification, which is reflected with additional −N = bond (quaternary nitrogen) at 399.9 eV in addition to the above four peaks [50]. Among these bonds, N-6 and N-5 can provide additional pseudocapacitance as electrochemically active sites. The N-Q bonds with three carbon atoms in a carbon matrix, which facilitates the electron transfer and greatly enhances the conductivity of the carbon matrix [52]. The O1s spectrum of MnO_2/HCS-30 (Fig. 5f) could be deconvoluted into four peaks at 529.8, 531.2, 531.7 and 534.1 eV. These peaks could be assigned to Mn−O−Mn, −COOH, Mn−O−H and C═O groups, respectively [53]. The presence of the Mn−O−Mn bond can be attributed to oxygen bonded with manganese in the MnO_2 crystal lattice. Furthermore, the contained Mn−O−H bond enhances the ion exchange and improves the electrochemical properties of the electrode material [54]. Fig. 5g shows the deconvoluted Mn 2p XPS spectrum for typical MnO_2 characteristics. In the MnO_2/HCS-30 sample, the two peaks appearing at 641.9 and 653.6 eV with a spin-energy splitting of 11.7 eV are severally pertained to the Mn $2p_{3/2}$ and Mn $2p_{1/2}$ orbits of Mn^{4+} [55].

3.2. Electrochemical measurements

The electrochemical behavior was first tested in a three-electrode set-up in 1 M Na_2SO_4 aqueous electrolyte. From Fig. 6a, we can clearly see that the curves of three samples have different integrated areas at the scan rate of 50 mV s^{-1}, indicating that the $KMnO_4$ concentration during hydrothermal reaction has an effect on the electrochemical performance of the material. The CV curves of the three composites all exhibit a nearly rectangular shape, which is a representation of the pseudo-capacitance properties of MnO_2 in the Na_2SO_4 electrolyte. In addition, MnO_2/HCS-30 has the largest integrated area at the scan rate of 50 mV s^{-1}, indicating the highest C_s values. The GCD curves are depicted in Fig. 6b. The C_s calculated according to Eq. (2) are 212 F g^{-1} (MnO_2/HCS-20), 255 F g^{-1} (MnO_2/HCS-30) and 137 F g^{-1} (MnO_2/HCS-40), respectively. In addition, the GCD curves of the three samples showed symmetry, indicating that the materials have good electrochemical reversibility. The best electrochemical performance of MnO_2/HCS-30 may be attributed to its more perfect thickness of the MnO_2 core-shell structure, which can provide more pseudo-capacitance contribution. Compared with MnO_2/HCS-30, the lower MnO_2 loading

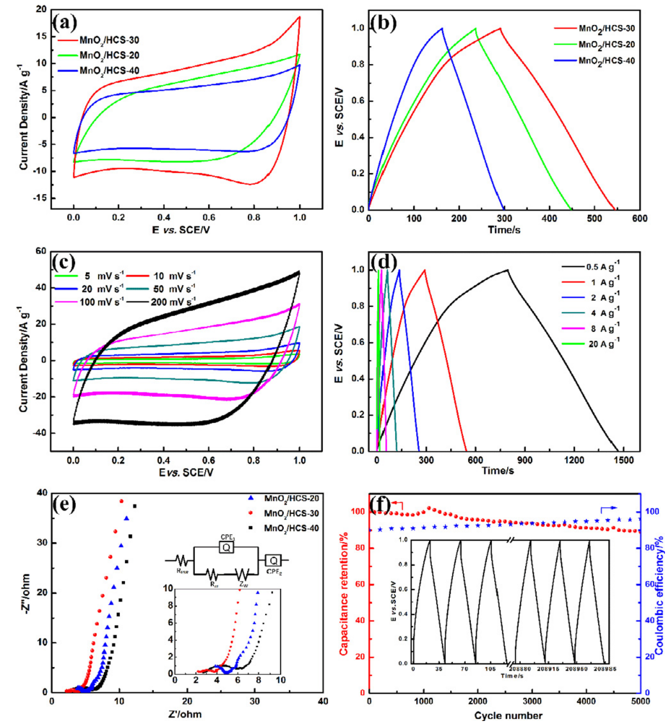

Fig. 6. The electrochemical performances of samples in 1 M Na_2SO_4 electrolyte. (a) CV curves at the scan rate of 50 mV s^{-1} (b) GCD curves at the current density of 1 A g^{-1} (c) CV curves at different scan rates. (d) GCD curves at different current densities of MnO_2/HCS-30. (e) Nyquist plots of samples. (f) Cycle life and coulombic efficiency of the MnO_2/HCS-30 at the current density of 10 A g^{-1}.

(MnO_2/HCS-20) makes it far from achieving the best electrochemical performance. The excessive deposition of MnO_2 (MnO_2/HCS-40) on the surface affects its electrical conductivity, resulting in a decreased performance. It is worth mentioning that the carbon sphere network based on the nitrogen doping can improve the wettability and electrical conductivity of the material in collaboration with a typical pseudo-capacitance material to achieve excellent electrochemical performance [56]. Fig. 6c shows the CV curves of the MnO_2/HCS-30 at scan rates from 5 to 200 mV s^{-1}. It can be seen that all the curves can still maintain approximately rectangular shape with the increase of the scan rate to 100 mV s^{-1}, indicating that the MnO_2/HCS-30 material has excellent electrochemical activity, high reversibility and a stable voltage window at 0–1 V. The curve begins to become distorted as the scan rate increases to 200 mV s^{-1}, which may be due to the fact that the internal resistance of the electrode hinders the charge collection and cation diffusion in the electrode at higher scan rates [57]. The CV curves of the MnO_2 electrode material show no peaks in the scan window, indicating that MnO_2 is charged/discharged at a pseudo-constant rate over the complete CV and is usually caused by the following two reactions:

$$(MnO_2)_{surface} + C^+ + e^- \leftrightarrow (MnOOC)_{surface} \tag{6}$$

$$MnO_2 + C^+ + e^- \leftrightarrow MnOOC \tag{7}$$

Briefly, one of these two mechanisms is the surface adsorption/desorption of electrolyte cations (C = H^+, Li^+, Na^+, K^+) on the surface of MnO_2 as shown in Eq. (6), and the other is the intercalation/deintercalation of electrolyte cations in MnO_2 as shown in Eq. (7) [58]. Fig. 6d displays the GCD curves of the MnO_2/HCS-30 at current densities from 0.5 to 20 A g^{-1}. The C_s are 336, 255, 236, 224, 216 and 176 F g^{-1} as the current densities increase to 0.5, 1, 2, 4, 8 and 20 A g^{-1}, respectively. Although the C_s decreases as the current density increases, it maintains the shape of an isosceles triangle, which indicates that the MnO_2/HCS-30 sample has excellent electrochemical reversibility and high Coulomb efficiency. The interface compatibility is one of the important factors that affects the property of a supercapacitor [59]. Fig. 6e presents the Nyquist plots of different samples. A magnified view of the Nyquist plots and corresponding equivalent circuit diagram are presented in the inset of the Fig. 6e. The equivalent circuit diagram is obtained by fitting, where R_{ESR}, R_{ct}, CPE, and Z_W correspond to the equivalent series resistance, charge transfer resistance, constant phase element and Warburg impedance, respectively. The illustrated curves have a similar shape, exhibiting a semicircular portion in the high-frequency region and an approximately vertical line in the low-frequency region. The cross-section semicircle reflects the values of the R_{ESR} and R_{ct}. The slope of the line represents the Warburg impedance of the diffusion behavior of the electrolyte in the electrode pores and the ions in the active material [60]. The R_{ESR} values of MnO_2/HCS-20, MnO_2/HCS-30, and MnO_2/HCS-40 are 2.4, 2.2 and 2.7 Ω, respectively, and the R_{ct} values are 2.2, 1.3 and 3.1 Ω, respectively. In addition, the curve of MnO_2/HCS-30 in the low-frequency region is also closer to vertical. The results above show that the MnO_2/HCS-30 has excellent ion diffusion and distribution properties.

As shown in Fig. 6f, the C_s of MnO_2/HCS-30 can still reach 89% of the initial capacitance after 5000 cycles of GCD at a current density of 10 A g^{-1}, indicating that the material has good cycle stability. It can be observed by the internal illustration that even though the decrease of charge/discharge time causes the attenuation of the capacitance, the symmetry of the curve shows only a slight change. This change may be due to the loss of the structural stability of the electrode material during the long cycle test [61]. It is worth mentioning that the Coulomb efficiency increased from 91% to 96% after 5000 cycles of charge-discharge cycle. It may be due to the electrode being more fully wetted in the electrolyte as the cycle progresses, resulting in a more complete cation adsorption/desorption and intercalation/deintercalation process on the MnO_2 surface.

The excellent electrochemical properties of the prepared MnO_2/HCS-30 electrodes may be attributed to: (1) HCS can not only provide strong mechanical support but also reduce the volume

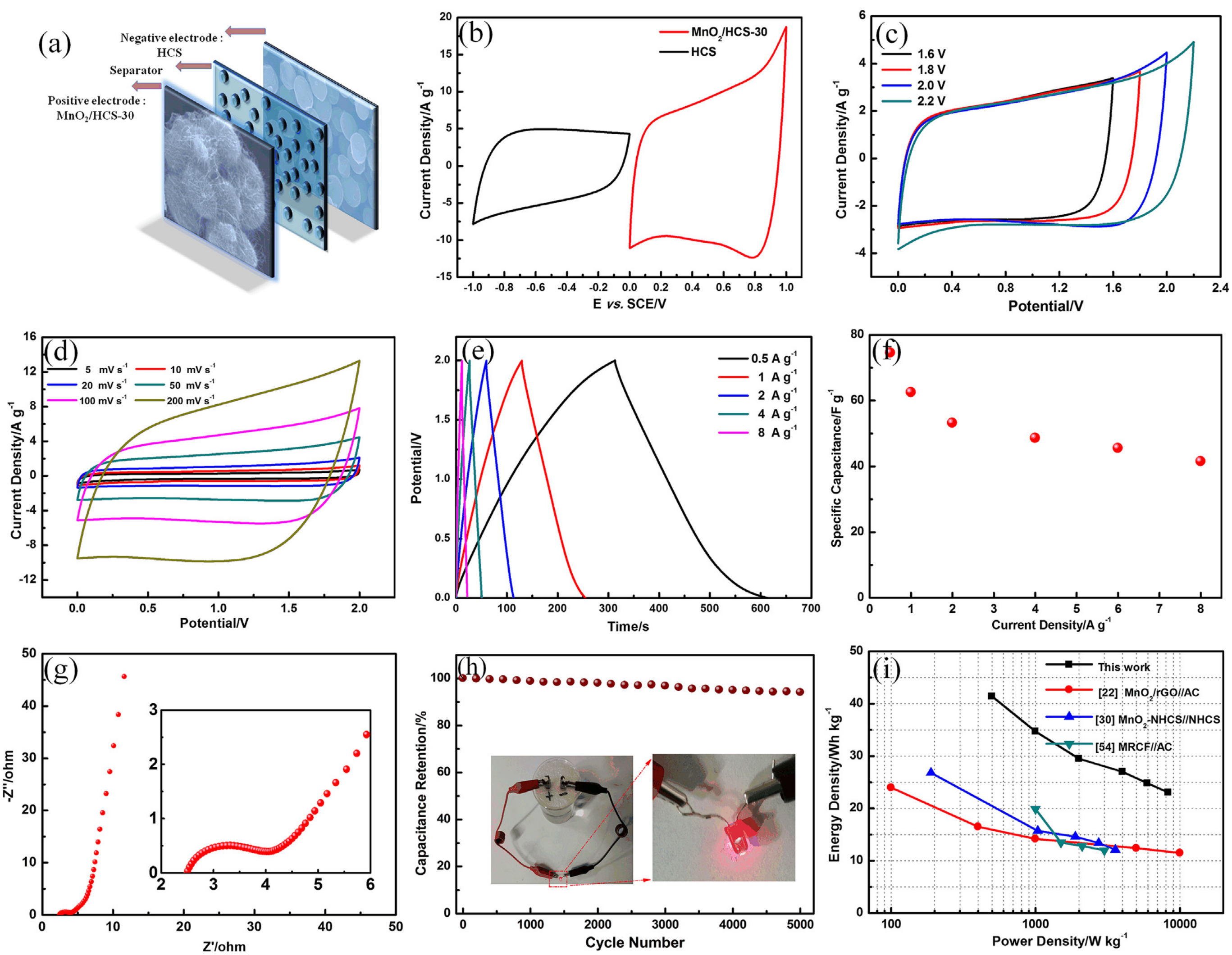

Fig. 7. The electrochemical performance of ASC in 1 M Na_2SO_4 aqueous electrolyte in a two electrode system: (a) The schematic diagram of the ASC. (b) Comparative CV curves of HCS and MnO_2/HCS-30 composite electrodes in a three-electrode system at a scan rate of 50 mV s^{-1}. (c) The CV curves of the ASC device in different operation voltage windows from 1.4 to 2.2 V at the scan rate of 50 mV s^{-1} (d) CV curves at different scan rate. (e) GCD curves at different current densities. (f) The gravimetric capacitance of the ASC device as a function of current density. (g) Nyquist plots of the ASC. (h) Cycling performance of the ASC device over 5000 cycles at a current density of 8 A g^{-1}. (i) The Ragone plot of the ASC.

Table 2
Comparison of asymmetric systems with MnO_2/Carbon-based positive electrode material.

Positive//negative electrodes	Specific capacitance ($F g^{-1}$)	Cell voltage (V)	Electrolyte	Capacitance retention	Cycle stability	Energy density ($Wh kg^{-1}$)	Ref.
MnO_2/rGO//AC	145 (0.5 $A g^{-1}$)	2.1	1 M Na_2SO_4	72% (0.2–5 $A g^{-1}$)	92% (1 $A g^{-1}$, 5000)	24	[22]
MnO_2–NHCS//NHCS	59.5 (0.5 $A g^{-1}$)	1.8	1 M Na_2SO_4	37% (0.5–5 $A g^{-1}$)	100% (1 $A g^{-1}$, 4000)	26.8	[30]
MRCF//AC	41.3 (0.3 $A g^{-1}$)	2.0	1 M Na_2SO_4	53% (0.3–3 $A g^{-1}$)	88% (2 $A g^{-1}$, 1000)	22.9	[54]
MnO_2/HCS-30//HCS	74.5 (0.5 $A g^{-1}$)	2.0	1 M Na_2SO_4	55.7% (0.5–8 $A g^{-1}$)	93.9% (1 $A g^{-1}$, 5000)	41.4	**This work**

expansion during the charge and discharge to enhance the cycle stability. In addition, this structure facilitates the electrolyte entering the electrochemical site and provides a short diffusion path length for adsorbing ions [62]. (2) The presence of wrinkles on the surface of the HCS can produce high electron conductivity and more reaction sites for faster ion and charge transfer rates [63]. (3) A large number of nitrogen-containing functional groups form a stable nitrogen doping in the carbon matrix after high-temperature carbonization, which can improve the wettability and provide more active sites [64]. (4) The MnO_2 nanowire is perfectly coated on the carbon shell, which facilitates the insertion of cations and provides a short diffusion path for electrolyte ions on the premise of minimizing the loss of conductivity.

In order to further characterize the electrochemical performance of the electrode material for practical applications, the ASC devices have been assembled by using MnO_2/HCS-30 and HCS as a positive electrode and negative electrode as shown in Fig. 7a. Stable CV curves (Fig. 7b) were obtained in the potential windows of −1 to 0 V for the HCS with ideal electric double-layer capacitor behavior and from 0 to 1 V for the MnO_2/HCS-30 with pseudocapacitive behavior, which is also consistent with the literature [61]. As shown in Fig. 7c, the assembled ASC can remain stable within a 2.0 V voltage window. However, when the voltage window reaches 2.2 V, the high potential current drastically increases due to the oxygen and/or hydrogen evolution reaction [65]. As can be seen in the Fig. 7d, the rectangular shape of the CV curves also remained unchanged when the scan rate was increased to 200 mV s^{-1}, indicating high rate capability. Furthermore, the GCD curves (Fig. 7e) of the ASC also show perfect highly linear and low IR drop with increasing the current density, indicating low internal series resistance and excellent reversibility [66]. Calculated from the GCD curves, the C_s values are summarized in Fig. 7f. The results showed that the C_s values of ASC are 74.5 F g^{-1} at 0.5 A g^{-1}. When the current density reaches 8 A g^{-1}, the capacitance is still 41.5 F g^{-1}, and the capacitance retention rate is 55.7%. The comparison of ASC performance in different literature is shown in Table 2.

EIS measurements were conducted using the assembled ASC device, as shown in Fig. 7g. Obviously, the EIS curve shows a semicircle diameter and a nearly vertical line, which is similar to the EIS curve of the three-electrode above. From the curve, it can be calculated that the interfacial resistance between the prepared electrode material and the Na_2SO_4 aqueous solution electrolyte is about 2.6 Ω, and the R_{ct} value is 1.7 Ω, showing a low resistance. In addition, the approximately vertical line at the low-frequency region also indicates a low ion diffusion resistance [67]. As shown in Fig. 7h, the prepared ASC device exhibits an excellent cycling stability with 93.9% capacitance retention after 5000 cycles. The internal illustration shows that the ASC can light up a 2.0 V light-emitting diode (LED) after charging, demonstrating the practicality of the material and proving to be an effective energy storage material. The Ragone plot (Fig. 7i) is commonly used to characterize the electrochemical performance of a supercapacitor device. From the curves, we can see that when the ASC reaches the maximum energy density of 41.4 Wh kg^{-1}, the power density is 500 W kg^{-1}, and when the maximum power density of 7901 W kg^{-1} is reached, the energy density value is 23.0 Wh kg^{-1}. In addition, it is worth mentioning that the use of HCS as a negative electrode instead of a commercial anode material in our device is more advantageous due to its lower cost and easier preparation.

4. Conclusion

In summary, we successfully prepared the nitrogen-doped porous hollow carbon spheres derived from the live yeast cell templates using hydrothermal pre-carbonization and pyrolysis carbonization method. During the *in-situ* deposition of MnO_2, the HCS acted as the template, nucleating agent, and carbon source. The MnO_2/HCS-30 (with a deposition thickness of 90 nm) exhibited an ultrahigh specific capacitance of 255 F g^{-1} at current density 1 A g^{-1} in 1 M Na_2SO_4 electrolyte. The assembled ASC employed the MnO_2/HCS-30 material as the positive electrode and the HCS as the negative electrode. The maximum energy density operating at the 2.0 V voltage window was 41.4 Wh kg^{-1} at a power density of 500 W kg^{-1} and still maintained 23.0 Wh kg^{-1} at a power density of 7901 W kg^{-1}. In addition, MnO_2/HCS-30 also exhibited a good cycling stability of 93.9% capacitance retention after 5000 cycles. This work may pave the way for the discovery of high-performance supercapacitor electrode materials based on the use of biological templates.

Acknowledgement

This work was supported by the National Natural Science Foundation of China (Grant No. 50802081, 51372138, 51772257) and the Outstanding Young Scientists' Award Fund of Shandong Province (2006BS04019).

References

[1] Z. Yang, J. Zhang, M.C.W. Kintner-Meyer, X. Lu, D. Choi, J.P. Lemmon, J. Liu, Electrochemical energy storage for green grid, Chem. Rev. 111 (2011) 3577–3613.
[2] S. Angaiah, V. Murugadoss, S. Arunachalam, S. Krishnan, Influence of various ionic liquids embedded electrospun polymer membrane electrolytes on the photovoltaic performance of DSSC, Eng. Sci. (2018), https://doi.org/10.30919/es8d756 in press.
[3] Q. Hou, J. Ren, H. Chen, P. Yang, Q. Shao, M. Zhao, X. Zhao, H. He, N. Wang, Q. Luo, Z. Guo, Synergistic Hematite-fullerene electron-extracting layers for improved efficiency and stability in perovskite solar cells, ChemElectroChem 5 (2018) 726–731.
[4] L. Yang, X. Wang, X. Mai, T. Wang, C. Wang, X. Li, V. Murugadoss, Q. Shao, S. Angaiah, Z. Guo, Constructing efficient mixed-ion perovskite solar cells based on TiO2 nanorod array, J. Colloid Interf. Sci. 534 (2019) 459–468.
[5] Q. Luo, H. Ma, Q. Hou, Y. Li, J. Ren, X. Dai, Z. Yao, Y. Zhou, L. Xiang, H. Du, H. He, N. Wang, K. Jiang, H. Lin, H. Zhang, Z. Guo, All-carbon-electrode-based endurable flexible perovskite solar cells, Adv. Funct. Mater. 28 (2018), 1706777.
[6] Q. Jiang, L. Wang, C. Yan, C. Liu, Z. Guo, N. Wang, Mesoporous TiO_2 vacancies modification for halide perovskite solar cells, Eng. Sci. 1 (2018) 64–68.
[7] T. Liu, K. Yu, L. Gao, H. Chen, N. Wang, L. Hao, T. Li, H. He, Z. Guo, Graphene quantum dots decorated SrRuO3 mesoporous film as an efficient counter electrode for high-performance dye-sensitized solar cells, J. Mater. Chem. 5 (2017) 17848–17855.
[8] M.M. Tavakoli, D. Prochowicz, P. Yadav, R. Tavakoli, M. Saliba, Zinc stannate nanorod as an electron transporting layer for highly efficient and hysteresis-less perovskite solar cells, Eng. Sci. 3 (2018) 48–53.

[9] Q. Luo, H. Ma, F. Hao, Q. Hou, J. Ren, L. Wu, Z. Yao, Y. Zhou, N. Wang, K. Jiang, H. Lin, Z. Guo, Carbon nanotube based inverted flexible perovskite solar cells with all-inorganic charge contacts, Adv. Funct. Mater. 27 (2017), 1703068.

[10] Q. Luo, H. Chen, Y. Lin, H. Du, Q. Hou, F. Hao, N. Wang, Z. Guo, J. Huang, Discrete iron(III) oxide nanoislands for efficient and photostable perovskite solar cells, Adv. Funct. Mater. 27 (2017), 1702090.

[11] L. Wei, K. Lozano, Y. Mao, Microwave popped Co(II)-graphene oxide hybrid: bifunctional catalyst for hydrogen evolution reaction and hydrogen storage, Eng. Sci. 3 (2018) 62–66, https://doi.org/10.30919/es8d723.

[12] H. Du, C. Zhao, J. Lin, Z. Hu, Q. Shao, J. Guo, B. Wang, D. Pan, E.K. Wujcik, Z. Guo, Carbon nanomaterials in direct liquid fuel cells, Chem. Rec. 18 (2018) 1365–1372.

[13] X. Lou, C. Lin, Q. Luo, J. Zhao, B. Wang, J. Li, Q. Shao, X. Guo, N. Wang, Z. Guo, Crystal-structure modification enhanced FeNb11O29 anodes for lithium-ion batteries, ChemElectroChem 4 (2017) 3171–3180.

[14] C. Lin, H. Hu, C. Cheng, K. Sun, X. Guo, Q. Shao, J. Li, N. Wang, Z. Guo, Nano-$TiNb_2O_7$/carbon nanotubes composite anode for enhanced lithium-ion storage, Electrochim. Acta 260 (2018) 65–72.

[15] L. Yan, H. Wang, D. Huang, H. Luo, Electrodes with high conductivities for high performance lithium/sodium ion batteries, Eng. Sci. 1 (2018) 4–20.

[16] Y. Guo, Y. Li, X. Lou, J. Guan, Y. Li, X. Mai, H. Liu, C.X. Zhao, N. Wang, C. Yan, G. Gao, H. Yuan, J. Dai, R. Su, Z. Guo, Improved extraction of cobalt and lithium by reductive acid from spent lithium-ion batteries via mechanical activation process, J. Mater. Sci. 53 (2018) 13790–13800.

[17] C. Liu, F. Li, L.-P. Ma, H.-M. Cheng, Advanced materials for energy storage, Adv. Mater. 22 (2010) E28-E62.

[18] J.-G. Wang, F. Kang, B. Wei, Engineering of MnO_2-based nanocomposites for high-performance supercapacitors, Prog. Mater. Sci. 74 (2015) 51–124.

[19] K. Jin, W. Zhang, Y. Wang, X. Guo, Z. Chen, L. Li, Y. Zhang, Z. Wang, J. Chen, L. Sun, T. Zhang, In-situ hybridization of polyaniline nanofibers on functionalized reduced graphene oxide films for high-performance supercapacitor, Electrochim. Acta 285 (2018) 221–229.

[20] X. Wang, X. Zeng, D. Cao, Biomass-derived nitrogen-doped porous carbons (NPC) and NPC/polyaniline composites as high performance supercapacitor materials, Eng. Sci. 1 (2018) 55–63.

[21] F. Ran, X. Yang, L. Shao, Recent progress in carbon-based nanoarchitectures for advanced supercapacitors, Adv. Compos. Hybrid. Mater. 1 (2018) 32–55.

[22] E. Miniach, A. Śliwak, A. Moyseowicz, L. Fernández-Garcia, Z. González, M. Granda, R. Menendez, G. Gryglewicz, MnO_2/thermally reduced graphene oxide composites for high-voltage asymmetric supercapacitors, Electrochim. Acta 240 (2017) 53–62.

[23] L.-H. Tseng, C.-H. Hsiao, D.D. Nguyen, P.-Y. Hsieh, C.-Y. Lee, N.-H. Tai, Activated carbon sandwiched manganese dioxide/graphene ternary composites for supercapacitor electrodes, Electrochim. Acta 266 (2018) 284–292.

[24] M. Liu, L. Gan, W. Xiong, Z. Xu, D. Zhu, L. Chen, Development of MnO_2/porous carbon microspheres with a partially graphitic structure for high performance supercapacitor electrodes, J. Mater. Chem. 2 (2014) 2555–2562.

[25] B. Mu, W. Zhang, W. Xu, A. Wang, Hollowed-out tubular carbon@MnO_2 hybrid composites with controlled morphology derived from kapok fibers for supercapacitor electrode materials, Electrochim. Acta 178 (2015) 709–720.

[26] D. Han, X. Jing, P. Xu, Y. Ding, J. Liu, Facile synthesis of hierarchical hollow ε-MnO_2 spheres and their application in supercapacitor electrodes, J. Solid State Chem. 218 (2014) 178–183.

[27] D. Feng, Z. Sun, Z. Huang, X. Cai, Y. Song, X. Liu, Highly loaded manganese oxide with high rate capability for capacitive applications, J. Power Sources 396 (2018) 238–245.

[28] Q. Zhang, L. Li, Y. Wang, Y. Chen, F. He, S. Gai, P. Yang, Uniform fibrous-structured hollow mesoporous carbon spheres for high-performance supercapacitor electrodes, Electrochim. Acta 176 (2015) 542–547.

[29] L. Shen, L. Du, S. Tan, Z. Zang, C. Zhao, W. Mai, Flexible electrochromic supercapacitor hybrid electrodes based on tungsten oxide films and silver nanowires, Chem. Commun. 52 (2016) 6296–6299.

[30] T. Liu, C. Jiang, W. You, J. Yu, Hierarchical porous C/MnO_2 composite hollow microspheres with enhanced supercapacitor performance, J. Mater. Chem. A 5 (2017) 8635–8643.

[31] W. Du, X. Wang, X. Ju, K. Xu, M. Gao, X. Zhang, Carbonized enteromorpha prolifera with porous architecture and its polyaniline composites as high-performance electrode materials for supercapacitors, J. Electroanal. Chem. 802 (2017) 15–21.

[32] Y.-K. Hou, G.-L. Pan, Y.-Y. Sun, X.-P. Gao, $LiMn_{0.8}Fe_{0.2}PO_4$/carbon nanospheres@graphene nanoribbons prepared by the biomineralization process as the cathode for lithium-ion batteries, ACS Appl. Mater. Interfaces 10 (2018) 16500–16510.

[33] J. Wu, A. Elliston, G. Le Gall, I.J. Colquhoun, S.R.A. Collins, J. Dicks, I.N. Roberts, K.W. Waldron, Yeast diversity in relation to the production of fuels and chemicals, Sci. Rep. 7 (2017) 14259.

[34] M. Di Serio, P. Aramo, E. de Alteriis, R. Tesser, E. Santacesaria, Quantitative analysis of the key factors affecting yeast growth, Ind. Eng. Chem. Res. 42 (2003) 5109–5116.

[35] M. Sauer, D. Porro, D. Mattanovich, P. Branduardi, 16 years research on lactic acid production with yeast – ready for the market? Biotechnol. Genet. Eng. Rev. 27 (2010) 229–256.

[36] M.E. Ersahin, R.K. Dereli, H. Ozgun, B.G. Donmez, I. Koyuncu, M. Altinbas, I. Ozturk, Source Based Characterization and Pollution Profile of a Baker's Yeast Industry, CLEAN–Soil, Air, Water, vol. 39, 2011, pp. 543–548.

[37] M. Yang, S. Zheng, Pollutant removal-oriented yeast biomass production from high-organic-strength industrial wastewater: a review, Biomass Bioenergy 64 (2014) 356–362.

[38] H. Wu, J. Geng, H. Ge, Z. Guo, Y. Wang, G. Zheng, Egg-derived mesoporous carbon microspheres as bifunctional oxygen evolution and oxygen reduction electrocatalysts, Adv. Energy Mater. 6 (2016), 1600794.

[39] A. Primo, P. Atienzar, E. Sanchez, J.M. Delgado, H. García, From biomass wastes to large-area, high-quality, N-doped graphene: catalyst-free carbonization of chitosan coatings on arbitrary substrates, Chem. Commun. 48 (2012) 9254–9256.

[40] Y. Xie, L. Fang, H. Cheng, C. Hu, H. Zhao, J. Xu, J. Fang, X. Lu, J. Zhang, Biological cell derived N-doped hollow porous carbon microspheres for lithium–sulfur batteries, J. Mater. Chem. 4 (2016) 15612–15620.

[41] N. Raghavan, S. Thangavel, G. Venugopal, A short review on preparation of graphene from waste and bioprecursors, Appl. Mater. Today 7 (2017) 246–254.

[42] C. Tang, H.-F. Wang, X. Chen, B.-Q. Li, T.-Z. Hou, B. Zhang, Q. Zhang, M.-M. Titirici, F. Wei, Topological defects in metal-free nanocarbon for oxygen electrocatalysis, Adv. Mater. 28 (2016) 6845–6851.

[43] B. Zhao, Q. Shao, L. Hao, L. Zhang, Z. Liu, B. Zhang, S. Ge, Z. Guo, Yeast-template synthesized Fe-doped cerium oxide hollow microspheres for visible photodegradation of acid orange 7, J. Colloid Interface Sci. 511 (2018) 39–47.

[44] D. Wang, L. Xu, Y. Wang, W. Xu, Rational synthesis of porous carbon nanocages and their potential application in high rate supercapacitors, J. Electroanal. Chem. 815 (2018) 166–174.

[45] Y. Zhang, S. Liu, X. Zheng, X. Wang, Y. Xu, H. Tang, F. Kang, Q.-H. Yang, J. Luo, Biomass organs control the porosity of their pyrolyzed carbon, Adv. Funct. Mater. 27 (2016), 1604687.

[46] G. Nie, X. Lu, J. Lei, C. Wang, Seed-assisted synthesis of hierarchical manganese dioxide/carbonaceous sphere composites with enhanced supercapacitor performance, Electrochim. Acta 180 (2015) 1033–1040.

[47] A. Talari, Z. Movasaghi, S. Rehman, I. Rehman, Raman spectroscopy of biological tissues, Appl. Spectrosc. Rev. 50 (2015) 46–111.

[48] Y. Liu, D. Yan, Y. Li, Z. Wu, R. Zhuo, S. Li, J. Feng, J. Wang, P. Yan, Z. Geng, Manganese dioxide nanosheet arrays grown on graphene oxide as an advanced electrode material for supercapacitors, Electrochim. Acta 117 (2014) 528–533.

[49] M. Dirican, M. Yanilmaz, X. Zhang, Free-standing polyaniline–porous carbon nanofiber electrodes for symmetric and asymmetric supercapacitors, RSC Adv. 4 (2014) 59427–59435.

[50] H. Li, B. Wang, X. He, J. Xiao, H. Zhang, Q. Liu, J. Liu, J. Wang, L. Liu, P. Wang, Composite of hierarchical interpenetrating 3D hollow carbon skeleton from lotus pollen and hexagonal MnO_2 nanosheets for high-performance supercapacitors, J. Mater. Chem. 3 (2015) 9754–9762.

[51] Q. Li, X. Bai, Q. Meng, T. Chen, W. Zhu, W. Yao, J. Lei, L. Zhang, X. Yang, X. Wei, T. Duan, Porous biochar generated from natural Amorphophallus konjac for high performance supercapacitors, Appl. Surf. Sci. 448 (2018) 16–22.

[52] D.K. Kim, N.D. Kim, S.-K. Park, K.-D. Seong, M. Hwang, N.-H. You, Y. Piao, Nitrogen doped carbon derived from polyimide/multiwall carbon nanotube composites for high performance flexible all-solid-state supercapacitors, J. Power Sources 380 (2018) 55–63.

[53] A. Pendashteh, E. Senokos, J. Palma, M. Anderson, J.J. Vilatela, R. Marcilla, Manganese dioxide decoration of macroscopic carbon nanotube fibers: from high-performance liquid-based to all-solid-state supercapacitors, J. Power Sources 372 (2017) 64–73.

[54] C. Zhao, Z. Ge, Y. Zhou, Y. Huang, G. Wang, X. Qian, Solar-assisting pyrolytically reclaimed carbon fiber and their hybrids of MnO_2/RCF for supercapacitor electrodes, Carbon 114 (2017) 230–241.

[55] H. Wang, F. Yin, B. Chen, G. Li, Synthesis of an ε-MnO_2/metal–organic-framework composite and its electrocatalysis towards oxygen reduction reaction in an alkaline electrolyte, J. Mater. Chem. 3 (2015) 16168–16176.

[56] Y. Li, X. Xu, Y. He, Y. Jiang, K. Lin, Nitrogen doped macroporous carbon as electrode materials for high capacity of supercapacitor, Polymers 9 (2017) 2.

[57] Z. Li, Y. Mi, X. Liu, S. Liu, S. Yang, J. Wang, Flexible graphene/MnO_2 composite papers for supercapacitor electrodes, J. Mater. Chem. 21 (2011) 14706–14711.

[58] X. Su, X. Yang, L. Yu, G. Cheng, H. Zhang, T. Lin, F.-H. Zhao, A facile one-pot hydrothermal synthesis of branched α-MnO_2 nanorods for supercapacitor application, CrystEngComm 17 (2015) 5970–5977.

[59] R. Na, X. Wang, N. Lu, G. Huo, H. Lin, G. Wang, Novel egg white gel polymer electrolyte and a green solid-state supercapacitor derived from the egg and rice waste, Electrochim. Acta 274 (2018) 316–325.

[60] Y. Zhao, Y. Meng, P. Jiang, Carbon@MnO_2 core–shell nanospheres for flexible high-performance supercapacitor electrode materials, J. Power Sources 259 (2014) 219–226.

[61] X. Li, Z. Wang, L. Guo, D. Han, B. Li, Z. Gong, Manganese oxide/hierarchical porous carbon nanocomposite from oily sludge for high-performance asymmetric supercapacitors, Electrochim. Acta 265 (2018) 71–77.

[62] M. Lin, B. Chen, X. Wu, J. Qian, L. Fei, W. Lu, L.W.H. Chan, J. Yuan, Controllable in situ synthesis of epsilon manganese dioxide hollow structure/RGO nanocomposites for high-performance supercapacitors, Nanoscale 8 (2016) 1854–1860.

[63] S. Yang, X. Song, P. Zhang, J. Sun, L. Gao, Self-assembled α-Fe_2O_3 mesocrystals/graphene nanohybrid for enhanced electrochemical capacitors, Small 10 (2014) 2270–2279.

[64] P. Yu, Z. Zhang, L. Zheng, F. Teng, L. Hu, X. Fang, A novel sustainable flour

derived hierarchical nitrogen-doped porous carbon/polyaniline electrode for advanced asymmetric supercapacitors, Adv. Energy Mater. 6 (2016), 1601111.
[65] B. Liu, Y. Liu, H. Chen, M. Yang, H. Li, Oxygen and nitrogen co-doped porous carbon nanosheets derived from Perilla frutescens for high volumetric performance supercapacitors, J. Power Sources 341 (2017) 309–317.
[66] C. Long, X. Chen, L. Jiang, L. Zhi, Z. Fan, Porous layer-stacking carbon derived from in-built template in biomass for high volumetric performance supercapacitors, Nano Energy 12 (2015) 141–151.
[67] M. Yang, S.B. Hong, B.G. Choi, Hierarchical core/shell structure of MnO_2@polyaniline composites grown on carbon fiber paper for application in pseudocapacitors, Phys. Chem. Chem. Phys. 17 (2015) 29874–29879.